Piezoelectric polarization field tuning Schottky barrier of Ni/Mn$_{0.2}$Cd$_{0.8}$S composite for hot electrons transfer to enhance photocatalytic hydrogen evolution

Haoqiang Feng, Yike Li [*], Yanan Han, Yongpan Gu, Zhongjun Li [*]

College of Chemistry, Zhengzhou University, Zhengzhou 450001, PR China

ARTICLE INFO

ABSTRACT

Coupling piezoelectric effect with local surface plasmon resonance (LSPR) for visible-light-driven photocatalytic hydrogen evolution is of great significance to realize the high-efficiency solar energy conversion. In this work, Ni/Mn$_{0.2}$Cd$_{0.8}$S plasmon piezo-photocatalysts were constructed by combining plasma metal Ni with structural distortion-enhanced Mn$_{0.2}$Cd$_{0.8}$S for piezo-photocatalytic hydrogen evolution. The influence of integrating plasma Ni with piezoelectric Mn$_{0.2}$Cd$_{0.8}$S on the photocatalytic performance was investigated together with the wavelength dependent experiments. Under simultaneous illumination and ultrasound, the optimized 1.5 wt %-Ni/Mn$_{0.2}$Cd$_{0.8}$S displayed ultrahigh piezo-photocatalytic hydrogen evolution rate of 72.38 mmol g^{-1} h^{-1}, which was approximately 11.8 and 25.0-fold that of Mn$_{0.2}$Cd$_{0.8}$S and CdS, respectively. The significantly enhanced performance was assigned to the coupling of piezoelectric and LSPR effect, through which the internal piezoelectric polarization field generated by Mn$_{0.2}$Cd$_{0.8}$S could change the local contact characteristics of Mn$_{0.2}$Cd$_{0.8}$S and Ni interface, decreasing the degree of upward bending of the band and reducing the Schottky barrier height, thus promoting the interfacial transfer of plasmon hot electrons for photocatalytic hydrogen evolution. This work provides a reliable reference for developing high-performance plasmonic piezo-photocatalysts materials based on piezoelectric and LSPR effect.

1. Introduction

The rapid development of industrialization and urbanization has led to the excessive consumption of traditional resources, resulting in energy shortages and environmental problems [1,2]. Exploring renewable clean energy is increasingly valued by researchers and enterprises [3,4]. In particular, as a green energy source with high-combustion value, easy storage and polluting-free, hydrogen has shown great economic and social benefits. Photocatalytic hydrogen evolution from water splitting is regarded as a promising approach for converting inexhaustible solar energy into hydrogen energy [5,6]. However, the serious photogenerated charge recombination both in the photocatalysts internal and on the surface is still a very significant disadvantage in the photocatalytic hydrogen evolution [7,8]. To overcome this challenging barrier, many strategies, including heterojunction construction [9], co-catalyst decoration [10] and surface defect engineering [11] have been investigated to improve the charges migration. However, the majority of research efforts focus on promoting the separation and transfer of photogenerated charges at the surface, while the recombination of photogenerated charges mainly occurs in the bulk phase of photocatalytic materials [12–14], which seriously restricts the photocatalytic efficiency.

Recently, the utilization of polarization field engineering to improve bulk phase photogenerated charges separation has aroused massive attention [15]. When piezoelectric semiconductor materials are exposed to both light and mechanical forces simultaneously, the light can excite the semiconductor materials, causing energy level transitions and generating photoinduced carriers. At the same time, the internal polarization electric field generated by external mechanical stimulation can accelerate the separation of photogenerated charge. Additionally, the piezoelectric polarization field can improve the charge transfer ability by adjusting the surface/interface band structure of the photocatalyst, thus further elevating the photocatalytic efficiency [16–18]. Due to these attractive properties, piezoelectric semiconductors, such as BaTiO$_3$ [19], SrTiO$_3$ [20], PbTiO$_3$ [21], CuInP$_2$S$_6$ [22], CdS [23] have been used for piezo-photocatalytic hydrogen evolution. Among them,

* Corresponding authors.
E-mail addresses: liyike@zzu.edu.cn (Y. Li), lizhongjun@zzu.edu.cn (Z. Li).

the non-centrosymmetric crystal structure wurtzite CdS, which exhibits both good piezoelectric and excellent photocatalytic hydrogen evolution properties, is favored as piezo-photocatalyst.

The piezoelectric performance of wurtzite CdS is mainly originated from the fact that the Cd-S bond length along the [0001] direction (2.605 Å) is slightly higher than that in other directions (2.601 Å), resulting in the distortion of CdS$_4$ tetrahedron and the generation of the local dipole moment when external strain is applied [24]. However, considering that the inherent polarity of wurtzite CdS is weak, it is necessary to use effective methods to modify wurtzite CdS so as to generate stronger polarization field, thus enhancing its piezo-photocatalytic performance. In this regard, Liu et al.[25] took one-dimensional CdS nanorods array as the research model to explore the piezo-photocatalytic hydrogen evolution from pure water, which showed that the CdS nanorods array was prone to deformation under the action of ultrasonic wave, could generate a strong piezoelectric polarization field to promote the photocatalytic hydrogen production. Huang et al.[26] prepared one-dimensional CdS nanorods for the piezoelectric catalytic hydrogen evolution, which exhibited nearly 2.8 times higher activity than spherical CdS, due to the stronger piezoelectric potential produced by CdS nanorods under pressure. Apart from regulating morphology, Zhang et al. [23] constructed phase junction with interfacial structural distortion between hexagonal CdS and cubic CdS to enhance the macroscopic polarization of wurtzite CdS and achieve an unprecedented piezo-photocatalytic hydrogen evolution in pure water. Using the similar tactic, Zhao et al.[27] improved the spontaneous polarization of CdS by introducing residual stress during the phase transition from cubic CdS to hexagon CdS, which generated a built-in electric field to promote charges migration and effectively enhanced the piezo-photoelectrochemical water splitting performance. Moreover, forming solid solution via ionic substitution to promote structural distortion degree was also considered to be an effective strategy to advance piezoelectric polarization of CdS. For instance, Huang et al. [28] prepared Cd$_x$Zn$_{1-x}$S solid solution nanorods for piezo-photocatalytic hydrogen evolution, the results indicated that Cd$_{0.4}$Zn$_{0.6}$S solid solution exhibited enhanced piezoelectric and photocatalytic performance compared with its single components. The above research on modulating the structure distortion of wurtzite CdS provided effective approaches that enable enhancing the piezo-photocatalytic performance.

Furthermore, coupling plasma metal with piezoelectric semiconductors to form more efficient visible-light-driven composites is a new research focus in the field of energy conversion [29–34]. To date, various types of plasmonic piezo-photocatalysts, including Au/ZnO [29], Al/BaTiO$_3$ [30], Au/AgNbO$_3$ [31], Au/CdS [32], Ag/g-C$_3$N$_4$ [33] and Au/MoS$_2$ [34] etc. have been successfully fabricated. The LSPR effect of plasma metals can broaden the light absorption range and generate favorable hot electrons, both are beneficial to the photocatalytic process [35–39]. Specifically, when the plasma metal is coupled to the piezoelectric semiconductor, a Schottky junction will be formed at the contact interface due to the difference in their work functions, which enables efficient migration of hot electrons driven by the created internal electric field into the conduction band of piezoelectric semiconductor to participate in the reduction reaction [40]. However, the formed Schottky junction also induces an upward bending of the semiconductor band edge resulting in a Schottky barrier, which features high contact resistance and hinders the flow of hot electrons across the interface for photocatalysis process [33]. Therefore, tuning the Schottky barrier height to facilitate the transport of hot electrons is very important for improving the performance of plasmonic piezo-photocatalytic systems. Fortunately, the internal polarization electric field could alter the local contact characteristics of the materials, leading to a change in interfacial band level [41–43], thus regulating the Schottky barrier height and the charge carrier transport process, which provides a highly desirable strategy to promote the interface transfer of hot electron for achieving the high-performance of photocatalytic

hydrogen evolution.

Based on the above considerations, in this work, using metal Ni as a plasmonic promoter, Ni/Mn$_{0.2}$Cd$_{0.8}$S plasmonic piezo-photocatalysts were successfully constructed by a facile solvothermal method followed with a photoreduction process. The two-step synthesis procedure of Ni/Mn$_{0.2}$Cd$_{0.8}$S was demonstrated in Fig. 1a. Briefly, the simple solvothermal process was used to synthesize Mn$_{0.2}$Cd$_{0.8}$S nanorod, and then the photo-reduction method was employed to anchor plasma metal Ni on Mn$_{0.2}$Cd$_{0.8}$S. Apart from its high activity and stability, plasmonic Ni exhibits wide-spectrum LSPR light absorption [35–39], which enables the investigation into the influence of integrating plasmonic metals with piezoelectric semiconductors on the photocatalytic performance in the wide spectrum. The research results indicated that under simultaneous illumination and ultrasound, the optimized 1.5 wt %-Ni/Mn$_{0.2}$Cd$_{0.8}$S composite displayed ultrahigh piezo-photocatalytic hydrogen evolution rate of 72.38 mmol g^{-1} h^{-1}, which was approximately 11.8 and 25.0-fold that of Mn$_{0.2}$Cd$_{0.8}$S and CdS, respectively. The significantly boosted photocatalytic performance for Ni/Mn$_{0.2}$Cd$_{0.8}$S composites was ascribed to the enhanced structural distortion of Mn$_{0.2}$Cd$_{0.8}$S and the reasonable coupling of its piezoelectric effect with the LSPR of metal Ni. The possible working mechanism was investigated and discussed based on piezo-photocatalytic and wavelength dependent hydrogen evolution experiments, photoelectrochemical tests, piezoresponse force microscopy (PFM), scanning Kelvin probe force microscopy (SKPFM) as well as density functional theory (DFT) calculation and finite element method.

2. Experimental section

2.1. Synthesis of CdS and Mn$_{0.2}$Cd$_{0.8}$S nanorods

CdS nanorods were synthesized through a solvothermal method. Typically, 5 mmol CdCl$_2$·5/2 H$_2$O and 10 mmol sublimed sulfur were dispersed in 50 mL diethylenetriamine and kept stirring for 1 h, and then poured into a 100 mL of PPL autoclave. The autoclave was sealed and placed in an oven for 24 h at 433 K. After cooling naturally, the precipitate was centrifugally separated, washed with deionized water and absolute ethanol until neutral, and dried at 333 K. The preparation of Mn$_{0.2}$Cd$_{0.8}$S nanorods was similar to that of CdS, except that the amount of metal precursor was changed to 4 mmol CdCl$_2$·5/2 H$_2$O and 1 mmol MnCl$_2$·4 H$_2$O. The actual atomic ratio of Mn^{2+}/Cd^{2+} in the as-prepared Mn$_{0.2}$Cd$_{0.8}$S solid solution was measured by inductively coupled plasma atomic emission spectroscopy (ICP-AES). The results of ICP-AES (Table S1) were consistent with the nominal values.

2.2. Synthesis of Ni/Mn$_{0.2}$Cd$_{0.8}$S composites

In detail, 100 mg Mn$_{0.2}$Cd$_{0.8}$S was added to a reactor containing 50 mL of aqueous ethanol (ethanol:water = 1:1) and sonicated for 30 min. Then, a certain volume of 1 mg/mL NiCl$_2$ aqueous solution was added into the above solution under stirring. The reaction system was purged with nitrogen for 20 min and illuminated under a 300 W Xenon lamp with a 420 nm cut-off filter for 15 min. The dark-green products were centrifugally separated, washed with deionized water and absolute ethanol, and dried at 333 K. The as-synthesized Ni/Mn$_{0.2}$Cd$_{0.8}$S samples were named as x-Ni/Mn$_{0.2}$Cd$_{0.8}$S in which x represented different content of Ni and x = 0.5, 1.0, 1.5 and 2.0 wt%.

2.3. Piezo-photocatalytic hydrogen evolution test

Piezo-photocatalytic hydrogen evolution experiments were measured on top-irradiation reaction vessels equipped with circulating cooling water. Light and ultrasonic conditions were achieved by a 300 W Xenon lamp (Beijing Perfectlight, PLS-SXE300, λ ≥ 420 nm) and an ultrasonic cleaner (KunShan, KQ-500DE, 40 KHz), respectively. Typically, 5 mg of the as-synthesized sample was uniformly dispersed in
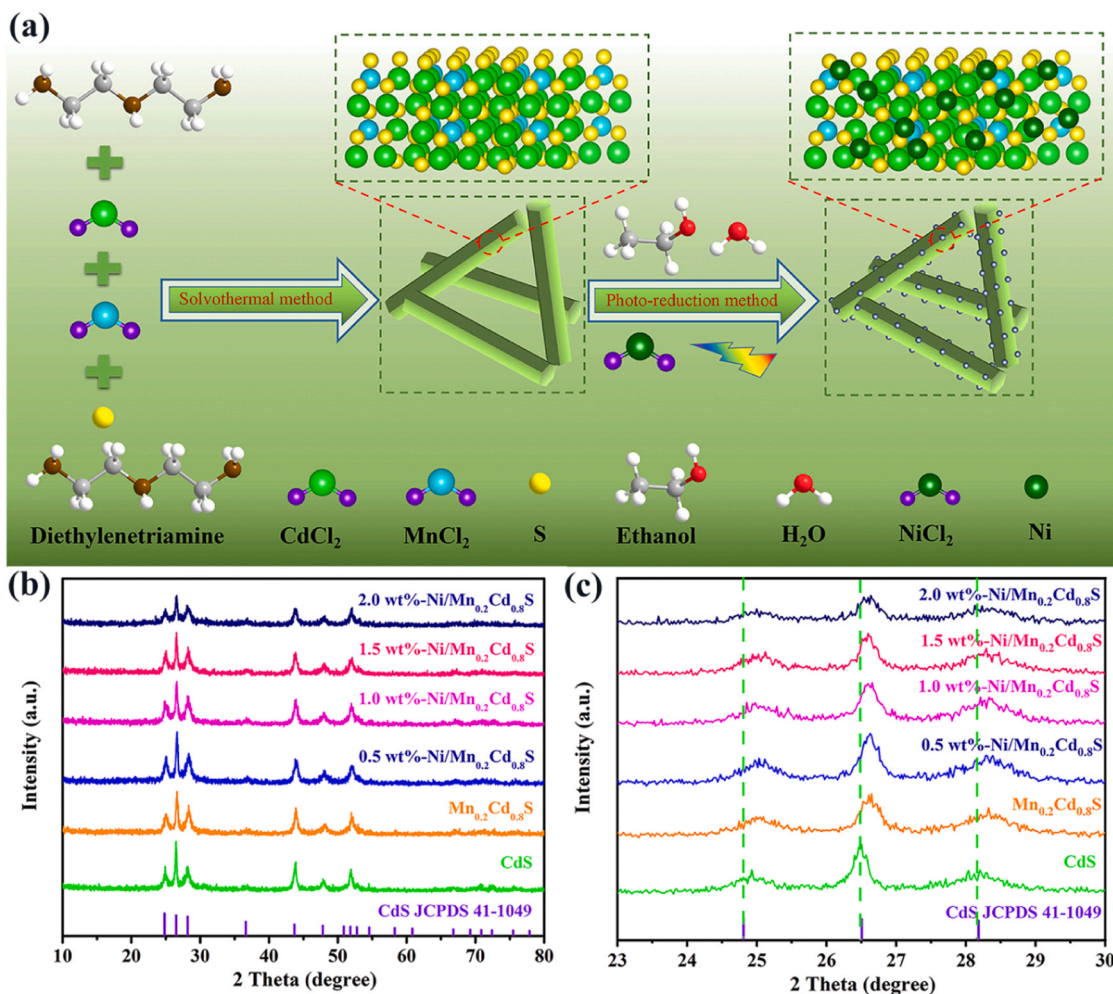
Fig. 1. (a) Schematic diagram of the synthesis procedure of the $Ni/Mn_{0.2}Cd_{0.8}S$ composites. (b) XRD patterns of CdS, $Mn_{0.2}Cd_{0.8}S$ and $Ni/Mn_{0.2}Cd_{0.8}S$ composites and the standard pattern of hexagonal CdS. (c) partial magnified portion of the XRD patterns with 2θ ranging from $23°$ to $30°$.

50 mL of 0.5 M Na_2S/Na_2SO_3 aqueous solution and sonicated for 5 min. Then, the reaction system was evacuated and pumped to atmospheric pressure with nitrogen. The reaction temperature was controlled at 25 $\pm$ 2 °C by circulating cooling water. In order to ensure the uniform distribution of H_2 gas in the reactor, the reactor was kept standing for 5 min after the reaction. The gases produced in the reactor were detected using gas chromatography (FULI, GC9790II).

The DFT calculations and characterization sections were presented in supplementary materials 2.4 and 2.5, respectively.

3. Results and discussion

3.1. Characterization of related catalysts

Fig. 1b displayed the XRD patterns of as-prepared samples. The XRD diffraction peaks of the as-synthesized CdS were coincided with the standard pattern of hexagonal CdS (JCPDS 41–1049). After introducing Mn^{2+} into the crystal lattice of CdS, the diffraction peak position of $Mn_{0.2}Cd_{0.8}S$ shifted to a higher angle than that of CdS (Fig. 1c), which was mainly ascribed to the fact that the radius of Mn^{2+} (0.46 Å) were smaller than that of Cd^{2+} (0.97 Å), resulting in smaller crystal plane spacing [44–46]. Because of the low content and amorphousness, the diffraction peaks of Ni could not be found in the XRD patterns of $Ni/Mn_{0.2}Cd_{0.8}S$ composites (Fig. 1b). Furthermore, the contents of Ni in the x-$Ni/Mn_{0.2}Cd_{0.8}S$ composites were determined by ICP-AES, which showed that the actual content of Ni in the composites was lower than

that of setting values and distributed at 0.18 to 1.01 wt% (Table S2).

The morphological characterization of relevant materials was carried out by scanning electron microscopy (SEM) and transmission electron microscopy (TEM), and the results were illustrated in Fig. 2, Fig. S1 and Fig. S2. As shown in Fig. 2a, CdS displayed well-crystallized nanorod morphology with the length and diameter approximately 200–400 nm and 40–60 nm, respectively. According to the SEM (Fig. 2b) and TEM (Fig. S1) images of $Mn_{0.2}Cd_{0.8}S$, the introduction of Mn^{2+} did not destroy the morphology of CdS. After the modification with plasma metal Ni, the morphology of 1.5 wt%-$Ni/Mn_{0.2}Cd_{0.8}S$ also did not change (Fig. S2 and Fig. 2c). The HRTEM image of 1.5 wt%-$Ni/Mn_{0.2}Cd_{0.8}S$ (Fig. 2d) showed lattice fringes of $Mn_{0.2}Cd_{0.8}S$ grown along the [0001] direction with an interplanar distance of 0.335 nm, corresponding to the (002) plane of $Mn_{0.2}Cd_{0.8}S$ [44–46], and the amorphous Ni was irregularly and discontinuously covered at the surface of $Mn_{0.2}Cd_{0.8}S$, as marked by green solid lines in Fig. 2d. Furthermore, the elemental maps results (Fig. 2e-i) indicated that Mn, Cd, S and Ni elements were uniformly distributed and well matched to each other in 1.5 wt%-$Ni/Mn_{0.2}Cd_{0.8}S$ composite.

The oxidation state and elemental compositions of the samples were characterized by XPS. The XPS survey spectra (Fig. S3) respectively showed the coexistence of related elements in the three samples and the high resolution XPS spectrum of relevant elements were given in Fig. 3. As displayed in Fig. 3a, two peaks of Cd 3d for CdS were located at 404.22 and 410.98 eV, which were in correspondence with the Cd $3d_{5/2}$ and Cd $3d_{3/2}$, respectively. The high resolution S 2p spectrum (Fig. 3b)
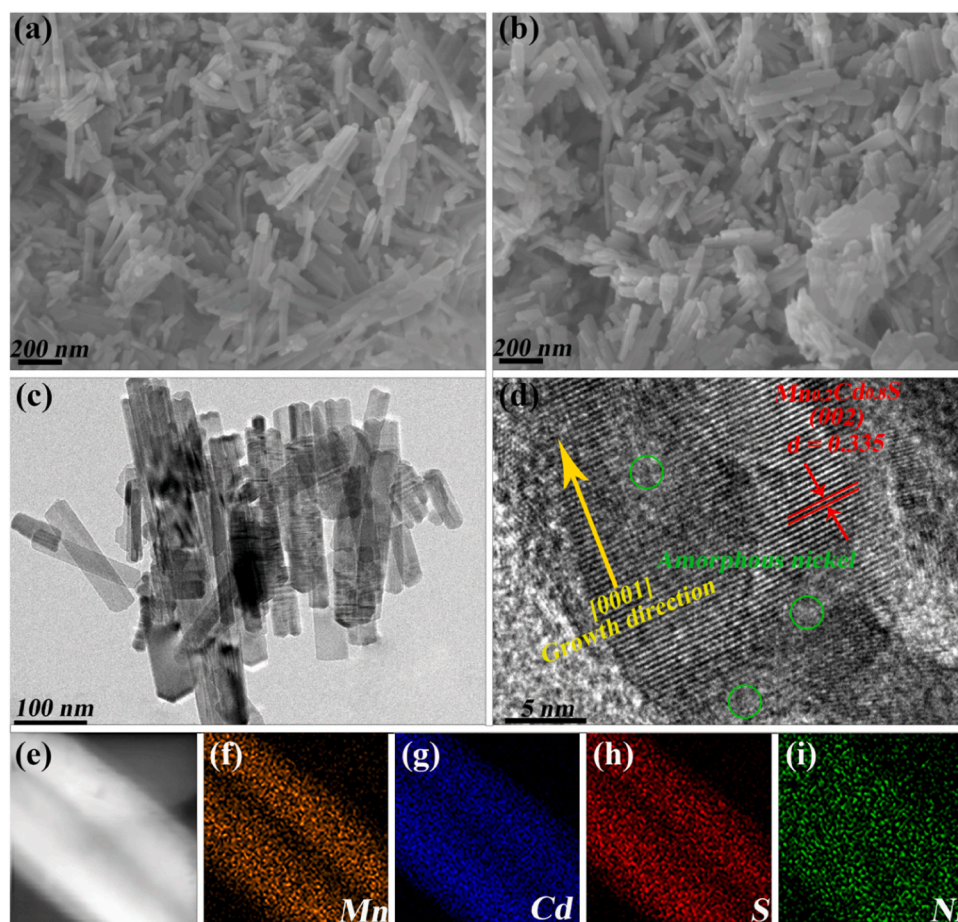
Fig. 2. SEM images of the (a) CdS and (b) $Mn_{0.2}Cd_{0.8}S$. (c) TEM image of 1.5 wt%-Ni/$Mn_{0.2}Cd_{0.8}S$. (d) HRTEM image of 1.5 wt%-Ni/$Mn_{0.2}Cd_{0.8}S$. (e) STEM-EDX image of 1.5 wt%-Ni/$Mn_{0.2}Cd_{0.8}S$ and the corresponding element mapping for (f) Mn, (g) Cd, (h) S, (i) Ni.

depicted two peaks at 160.64 and 161.92 eV, belonging to the S $2p_{3/2}$ and S $2p_{1/2}$, respectively. The peaks of Cd 3d for $Mn_{0.2}Cd_{0.8}S$ were situated at 404.04 and 410.77 eV, and the peaks of S 2p for $Mn_{0.2}Cd_{0.8}S$ were located at 160.45 and 161.72 eV. Obviously, the peak positions of Cd 3d and S 2p in $Mn_{0.2}Cd_{0.8}S$ solid solution shifted to low binding energy values compared with those of CdS, which should be attributed to the charge redistribution during the formation of the solid solution [28]. For 1.5 wt%-Ni/$Mn_{0.2}Cd_{0.8}S$, the high resolution Mn 2p spectrum (Fig. 3c) depicted two peaks at 640.56 and 651.47 eV, corresponding to the Mn $2p_{3/2}$ and Mn $2p_{1/2}$, respectively. Two peaks of Cd 3d were located at 404.24 and 410.98 eV, and those of S 2p at 160.67 and 161.89 eV. The peak positions of Cd 3d, Mn 2p and S 2p in 1.5 wt%-Ni/$Mn_{0.2}Cd_{0.8}S$ shifted to high binding energies values compared with those of $Mn_{0.2}Cd_{0.8}S$ due to the transfer of electrons from $Mn_{0.2}Cd_{0.8}S$ with high Fermi levels to Ni (Fig. S4) during the formation of Schottky barrier [47]. Obviously, the Ni 2p spectrum of 1.5 wt%-Ni/$Mn_{0.2}Cd_{0.8}S$ contained five peaks located at 852.10, 854.70, 860.58, 872.08 and 877.50 eV, as displayed in Fig. 3d. Among them, the peak at 852.10 eV belonged to Ni^0, while the peaks at 854.70, 860.58, 872.08 and 877.50 eV, were mainly attributed to the presence of Ni-O due to the oxidation of metallic nickel on the surface of $Mn_{0.2}Cd_{0.8}S$ in the testing process, similar situations were reported by other groups [48–50].

3.2. Piezoelectric properties of related catalysts

PFM was used to characterize the local piezoelectric response of CdS, $Mn_{0.2}Cd_{0.8}S$ and 1.5 wt%-Ni/$Mn_{0.2}Cd_{0.8}S$ on ITO film substrates. From the corresponding morphology (Fig. 4a, d, g), amplitude (Fig. 4b, e, h) and phase images (Fig. 4c, f, i), it could be observed that the three samples exhibited clearly regional color contrast compared to the ITO substrate without piezoelectric characteristics, indicating the existence of vertical polarization components. The amplitude and phase changes could be clearly observed in the CdS, $Mn_{0.2}Cd_{0.8}S$ and 1.5 wt%-Ni/$Mn_{0.2}Cd_{0.8}S$ sample regions. The amplitude differences of CdS, $Mn_{0.2}Cd_{0.8}S$ and 1.5 wt%-Ni/$Mn_{0.2}Cd_{0.8}S$ were 8.3, 10.9 and 8.3 pm, respectively, and the phase changes were 26.0°, 25.1°, and 24.5° for CdS, $Mn_{0.2}Cd_{0.8}S$ and 1.5 wt%-Ni/$Mn_{0.2}Cd_{0.8}S$, separately. The above results demonstrated that the three samples possessed excellent piezoelectric responses under $+ 10$ V voltage [51]. The typical local piezoelectric butterfly curves and phase hysteresis loops with changes of $\approx 169°$, $\approx 175°$ and $\approx 185°$ for CdS, $Mn_{0.2}Cd_{0.8}S$ and 1.5 wt%-Ni/$Mn_{0.2}Cd_{0.8}S$, respectively, at ± 10 V bias voltage field (Fig. S5), which indicated that 1.5 wt%-Ni/$Mn_{0.2}Cd_{0.8}S$ had the higher piezoelectric response [52]. Furthermore, using a scanning area of 5×5 μm^2, the scanning Kelvin probe force microscope (SKPFM) was used to measure the surface piezoelectric potential of 1.5 wt%-Ni/$Mn_{0.2}Cd_{0.8}S$ in a contactless mode. The 3D images of morphology and relevant surface piezoelectric potentials in dark and illumination conditions were shown in Fig. 5a-b and Fig. 5d-e, respectively. Fig. 5c displayed the surface piezoelectric potential (≈ 874, ≈ 871, ≈ 877 and ≈ 871 mV) along the red line (A-B) in Fig. 5b under dark condition, which was decreased (≈ 756, ≈ 767, ≈ 762 and ≈ 758 mV) under illumination as shown in Fig. 5f. The decline in surface potential could be attributed to the generation of charge carriers by both the photo-induce and LSPR under illumination, resulting in charge shielding effect, which was similar to the phenomenon in other works [28].
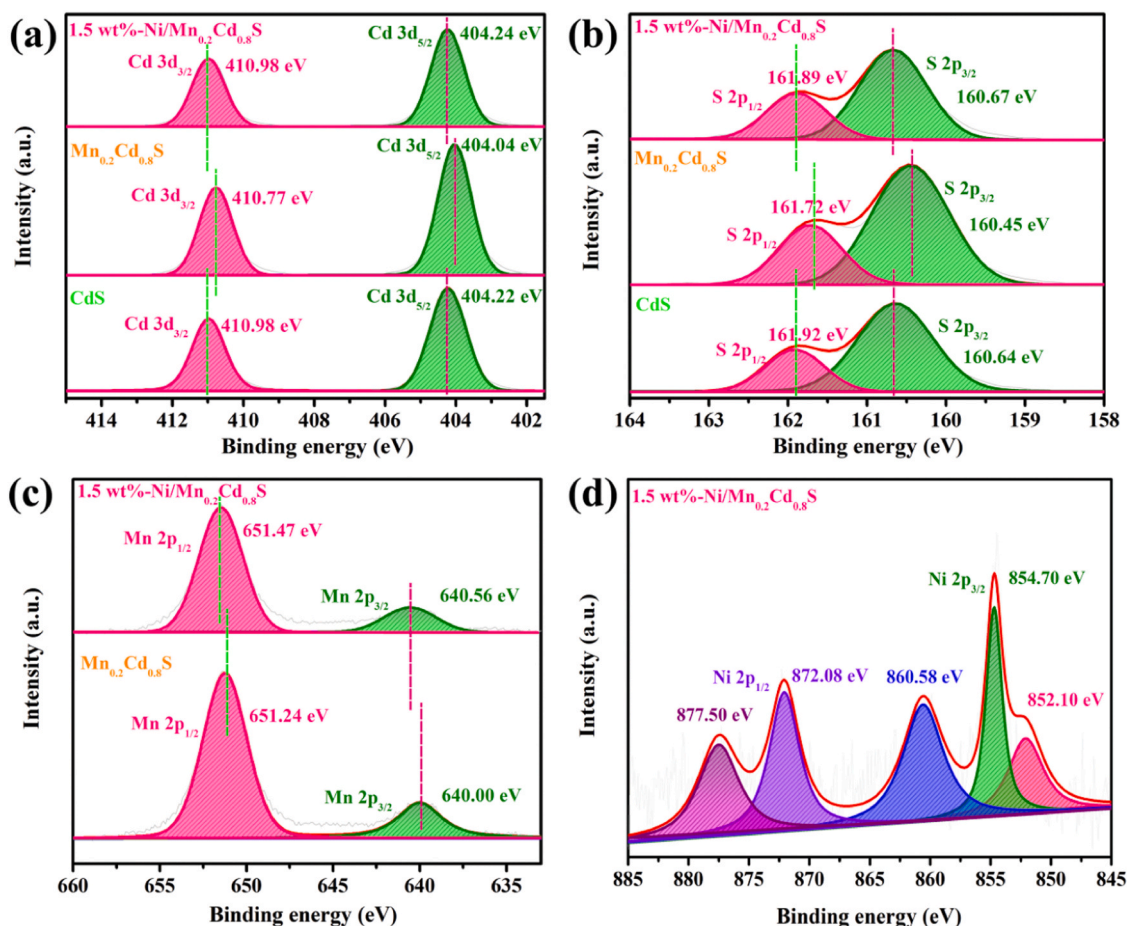
Fig. 3. High resolution XPS spectra of (a) Cd 3d, (b) S 2p, (c) Mn 2p and (d) Ni 2p for relevant samples.

3.3. Enhanced macroscopic polarization of $Mn_{0.2}Cd_{0.8}S$

The dipole moment and polyhedral distortion index were used to evaluate and analyze the macroscopic polarization of CdS and $Mn_{0.2}Cd_{0.8}S$. The optimized structural model of wurtzite $Cd_{10}S_{10}$ was shown in Fig. 6a. By contrast, 2 Mn atoms were used to replace 2 Cd atoms in $Cd_{10}S_{10}$ protocell to form $Mn_2Cd_8S_{10}$ solid solution structural model, and the stable structure of $Mn_2Cd_8S_{10}$ was displayed in Fig. 6b. As expected, the dipole moment exhibited a dependence on the symmetry of the lattice structure, with the values of -11.75 and -21.68 D in the [0001] direction for $Cd_{10}S_{10}$ and $Mn_2Cd_8S_{10}$, respectively. Furthermore, polyhedral distortion could destroy the symmetry of coordination environment in crystal structure, leading to the enhancement of macroscopic polarization [23], which was further analyzed by polyhedral distortion index D. The average polyhedral distortion index of CdS_4 tetrahedron in $Mn_{0.2}Cd_{0.8}S$ was determined to be 1.6×10^{-2}, which was larger than that in CdS (1.1×10^{-3}), and the detailed data were depicted in Table S3 and Table S4. The above results showed that compared with CdS, $Mn_{0.2}Cd_{0.8}S$ exhibited enhanced macroscopic polarization, which could induce a stronger piezoelectric polarization field for improving the separation efficiency of bulk phase photogenerated charge, and hence promoting the piezo-photocatalytic hydrogen production activity.

3.4. Finite element simulation of $Mn_{0.2}Cd_{0.8}S$ and plasma Ni

In order to understand the influence of acoustic pressure and impact force caused by acoustic cavitation on piezoelectric materials under the action of ultrasonic, the Finite element simulation (COMSOL Multiphysics 6.0) was carried out for $Mn_{0.2}Cd_{0.8}S$ nanorod. According to the

obtained $Mn_{0.2}Cd_{0.8}S$ hybrid structure and morphology sizes, a cylinder with a diameter of 50 nm and a height of 300 nm was defined as the geometric parameters for modeling. Fig. 7 showed the 2D and 3D distributions of stress, potential, sound pressure and sound pressure level along the z axis on the surface of $Mn_{0.2}Cd_{0.8}S$ under the real simulation model. It could be seen that $Mn_{0.2}Cd_{0.8}S$ nanorod could generate stress deformation and surface potential difference under the action of ultrasonic wave, thus producing piezoelectric polarization to accelerate the separation of bulk phase photogenerated carriers.

In addition, electromagnetic simulations of the plasma metal Ni on the $Mn_{0.2}Cd_{0.8}S$ under different irradiation of monochromatic light were carried out. From Fig. 8, it's clear that the electromagnetic field over the Ni/$Mn_{0.2}Cd_{0.8}S$ was enhanced with different irradiation of monochromatic light. The LSPR of the plasma metal Ni exhibited 10 times higher electric field than the original input, therefore, the hot electrons excited by plasma metal Ni could be transferred to nearby $Mn_{0.2}Cd_{0.8}S$ through numerous electric field enhancement sites [42]. It could be speculated that the LSPR effect of plasma Ni had an important influence on the enhancement of piezo-photocatalytic hydrogen production performance of $Mn_{0.2}Cd_{0.8}S$.

3.5. Optical property and photoelectrochemical analysis

The UV-Vis-NIR DRS of CdS, $Mn_{0.2}Cd_{0.8}S$ and Ni/$Mn_{0.2}Cd_{0.8}S$ were illustrated in Fig. 9a. Compared to CdS, the absorption band edge of $Mn_{0.2}Cd_{0.8}S$ displayed the red shift to the long wave direction with the light absorption obviously enhanced in the visible region due to the introduction of Mn^{2+}. After the deposition of plasma metal Ni, the Ni/$Mn_{0.2}Cd_{0.8}S$ exhibited a further enhanced light absorption in the visible and near infrared regions, and the intensity of which was gradually
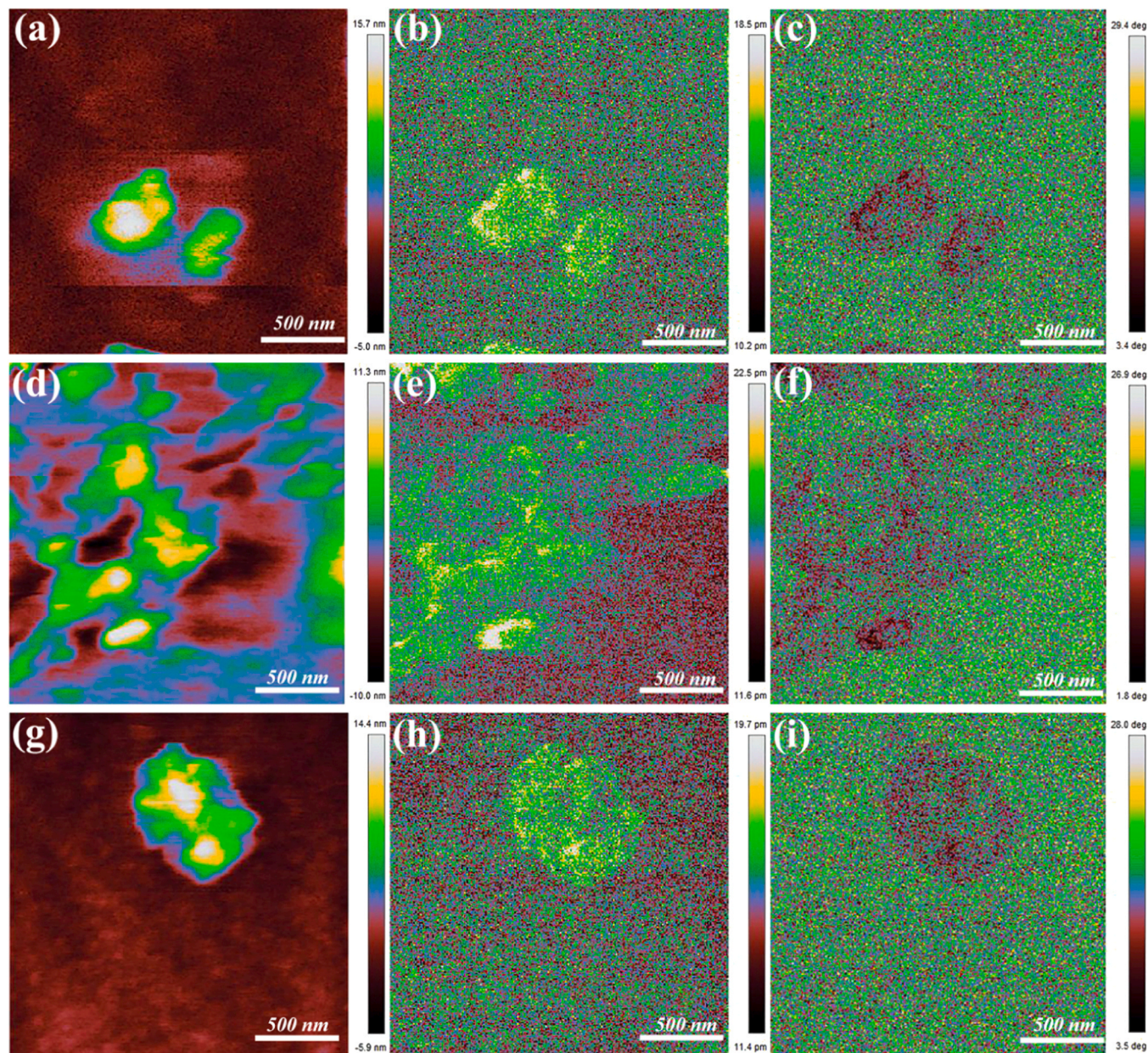
Fig. 4. The morphology, vertical piezoresponse amplitude and phase images of (a-c) CdS, (d-f) $Mn_{0.2}Cd_{0.8}S$ and (g-i) 1.5 wt%-Ni/$Mn_{0.2}Cd_{0.8}S$.

raised with increasing the amount of Ni.

PL and TRPL were applied to study the recombination rate of photogenerated carriers. As shown in Fig. 9b, the CdS, $Mn_{0.2}Cd_{0.8}S$ and Ni/$Mn_{0.2}Cd_{0.8}S$ displayed distinct emission peaks at 540 nm with the excitation wavelength of 331 nm. Pure CdS showed the highest emission intensity, followed by $Mn_{0.2}Cd_{0.8}S$, whereas 1.5 wt%-Ni/$Mn_{0.2}Cd_{0.8}S$ presented the weakest one, indicating that the introduction of plasma metal Ni contributed to the inhibition of photogenerated charge recombination. The emission decay curves of all samples were obtained by fitting the short-life component τ_1 and the long-life component τ_2 with double-exponential function (Fig. 9c and Fig. S6-S8). The decay lifetime was calculated according to the equation below: $\tau_{ave} = (A_1 * \tau_1^2 + A_2 * \tau_2^2)/(\tau_1 * A_1 + \tau_2 * A_2)$. After introducing Mn^{2+} and subsequently plasma Ni, the average decay lifetime of CdS decreased from 6.89 to 3.55 and then 3.46 ns (Table S5), reflecting that the charge separations were effectually impelled in 1.5 wt%-Ni/$Mn_{0.2}Cd_{0.8}S$.

Transient photocurrent and electrochemical impedance spectroscopy (EIS) were applied to analyze the photogenerated carrier migration and separation efficiency of CdS, $Mn_{0.2}Cd_{0.8}S$ and 1.5 wt%-Ni/$Mn_{0.2}Cd_{0.8}S$. It could be seen from Fig. 9d that among the three samples, 1.5 wt%-Ni/$Mn_{0.2}Cd_{0.8}S$ possessed the highest photocurrent density with and without ultrasonic, exhibiting remarkably enhanced separation and transportation efficiency of charge carriers. Moreover, compared with that of CdS, the photocurrent density of both $Mn_{0.2}Cd_{0.8}S$ and 1.5 wt%-Ni/$Mn_{0.2}Cd_{0.8}S$ was obviously raised by ultrasonic, and the increase in photocurrent for 1.5 wt%-Ni/$Mn_{0.2}Cd_{0.8}S$ was more significant than that for $Mn_{0.2}Cd_{0.8}S$, which indicated that the synergy of $Mn_{0.2}Cd_{0.8}S$ piezoelectric and Ni LSPR effect was conducive to the separate and transfer of photogenerated charges. Fig. 9e displayed the EIS Nyquist plots of CdS, $Mn_{0.2}Cd_{0.8}S$ and 1.5 wt%-Ni/$Mn_{0.2}Cd_{0.8}S$ with and without ultrasonic. The results showed that although 1.5 wt%-Ni/$Mn_{0.2}Cd_{0.8}S$ had a smallest radius no matter with or without ultrasonic stimulation, the extent of radius reduction from CdS to $Mn_{0.2}Cd_{0.8}S$ was more noticeable than that from $Mn_{0.2}Cd_{0.8}S$ to 1.5 wt%-Ni/$Mn_{0.2}Cd_{0.8}S$, indicating the introduction of Mn^{2+} in CdS was beneficial to reducing the interface resistance of charge transfers. In
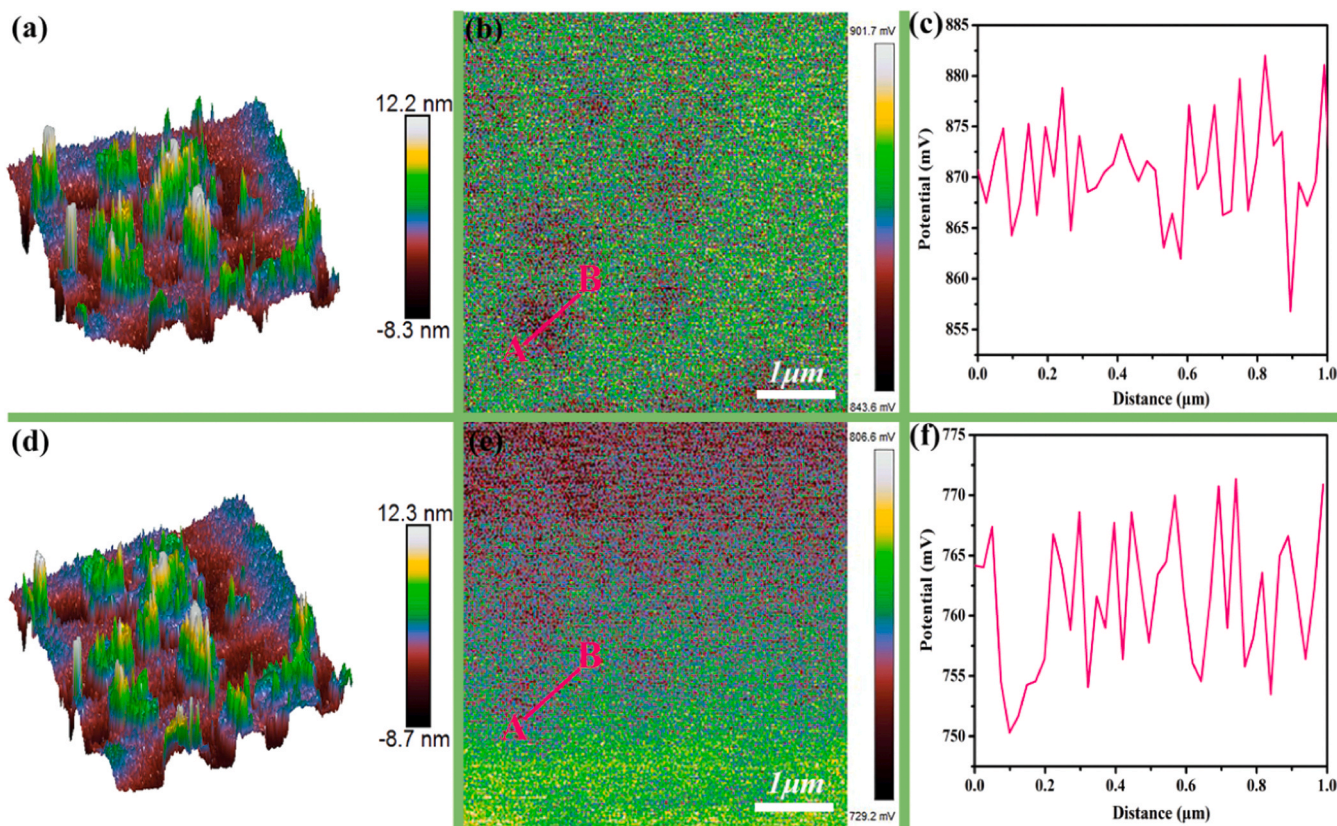
Fig. 5. 3D images of morphology and relevant surficial piezoelectric potentials of 1.5 wt%-Ni/$Mn_{0.2}Cd_{0.8}$S in (a–c) dark and (d–f) illumination conditions.
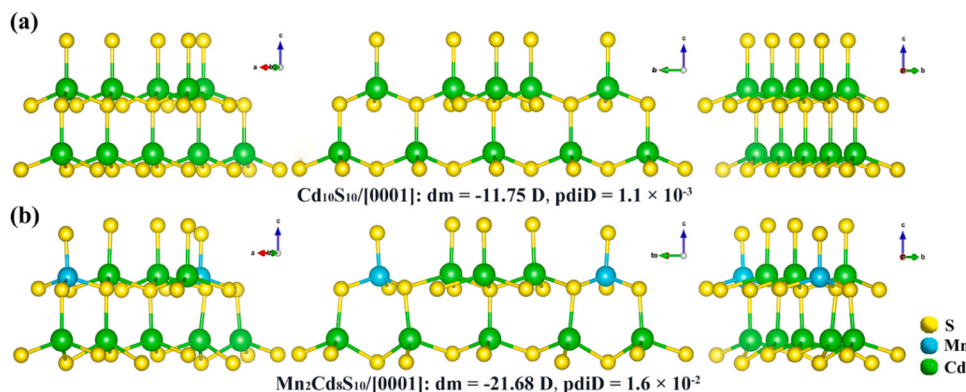

Fig. 6. The optimized structures of (a) $Cd_{10}S_{10}$ and (b) $Mn_2Cd_8S_{10}$ in the DFT calculations as well as the dipole moment (dm) and polyhedral distortion index D (pdiD) in $Cd_{10}S_{10}$ and $Mn_2Cd_8S_{10}$ along the [0001] direction.

addition, the decrease of interface resistance under ultrasonic condition was also related to the acceleration of interface carrier migration driven by piezoelectric polarization field [32].

In order to further understand the mechanism of piezoelectric effect enhancing photogenerated charge separation, the band structure was studied by Mott-Schottky test. From the Mott-Schottky plots of the $Mn_{0.2}Cd_{0.8}$S (Fig. 9f) and 1.5 wt%-Ni/$Mn_{0.2}Cd_{0.8}$S (Fig. 9g), the flat-band potential (V_{fb}) for $Mn_{0.2}Cd_{0.8}$S and 1.5 wt%-Ni/$Mn_{0.2}Cd_{0.8}$S were determined to be −0.70 and −1.10 V (vs. Ag/AgCl at pH=7), respectively. Considering that all curves exhibited positive slope typical of n-type semiconductors, the conduction band positions (E_{CB}) of the related samples were calculated to be −0.80 and −1.20 V (vs. Ag/AgCl at pH=7), respectively. Thus the E_{CB} (vs. NHE) of $Mn_{0.2}Cd_{0.8}$S and 1.5 wt%-Ni/$Mn_{0.2}Cd_{0.8}$S was ascertained to be −0.60 and −1.00 according to the conversion relation of $E_{NHE} = E_{Ag/AgCl} + 0.197$. This result

indicated that the contact of Ni with $Mn_{0.2}Cd_{0.8}$S resulted in the negative shift of the E_{CB} of $Mn_{0.2}Cd_{0.8}$S by 0.40 V, which was attributed to the charge transfer at the interface of $Mn_{0.2}Cd_{0.8}$S and Ni during the formation of Schottky barriers. Additionally, from the Mott−Schottky curve of 1.5 wt%-Ni/$Mn_{0.2}Cd_{0.8}$S measured in the presence of ultrasonic (Fig. 9h), the E_{CB} of 1.5 wt%-Ni/$Mn_{0.2}Cd_{0.8}$S was calculated to be −0.86 V (vs. NHE) for the case with ultrasonic. The potential difference of 0.14 V (ΔΦ) could be observed, which was reasonably attributed to the band bending caused by the ultrasonic induced piezoelectric polarization field [53]. The band gap energy (E_g) of $Mn_{0.2}Cd_{0.8}$S and 1.5 wt%-Ni/$Mn_{0.2}Cd_{0.8}$S were respectively estimated to be 2.28 and 2.25 eV, as illustrated in Fig. 9i. Based on the equation of $E_{CB} = E_{VB} − E_g$, the valence band potential (E_{VB}) of $Mn_{0.2}Cd_{0.8}$S and 1.5 wt%-Ni/$Mn_{0.2}Cd_{0.8}$S were calculated to be 1.68 and 1.25 V (vs. NHE), respectively.
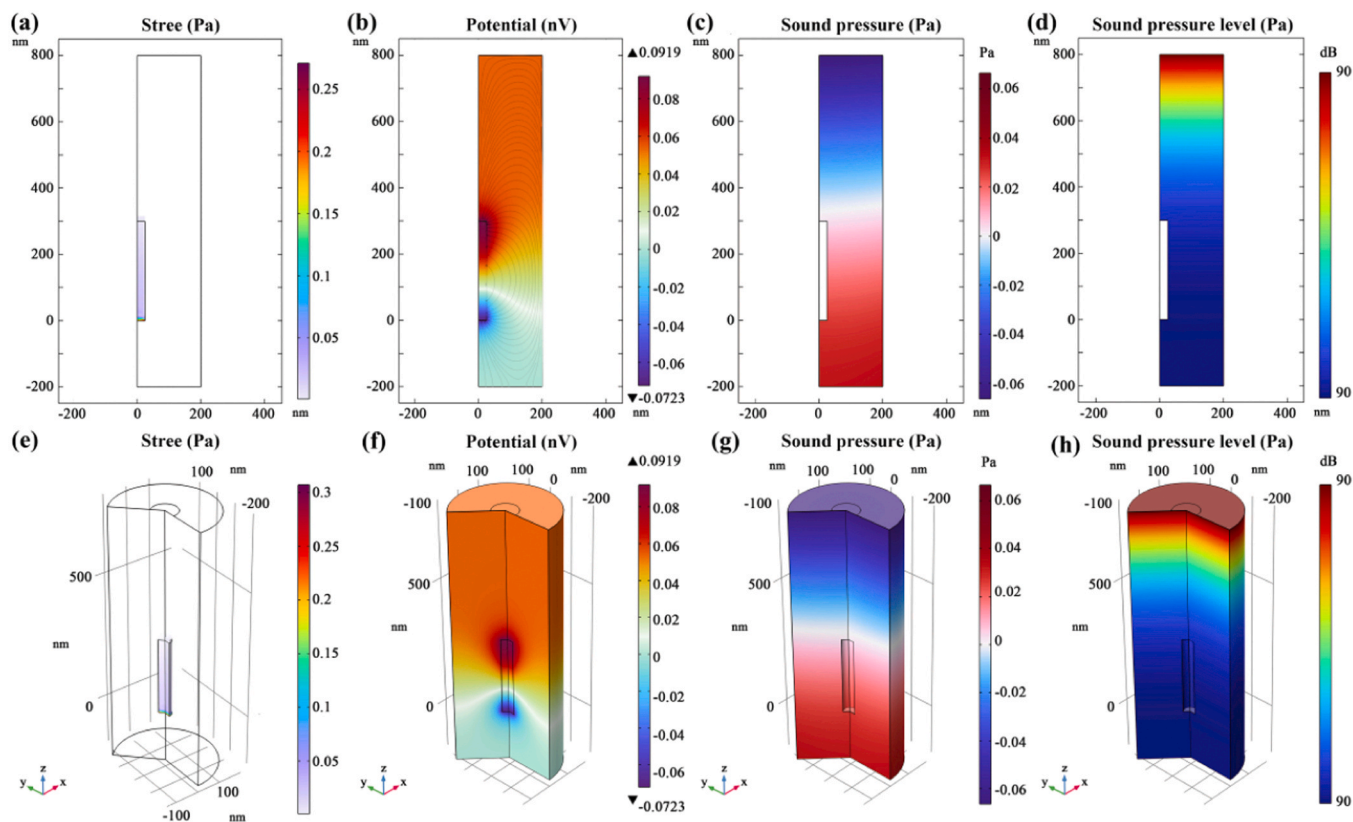
Fig. 7. The 2D (a-d) and 3D (e-h) distributions of stress, potential, sound pressure and sound pressure level along the z axis on the surface of $Mn_{0.2}Cd_{0.8}S$ under the real simulation model.

3.6. Piezo-photocatalytic and wavelength dependence hydrogen evolution

As displayed in Fig. S9 and Fig. 10, the hydrogen evolution performance of as-prepared materials was tested under ultrasonic vibration (ultrasonic, 200 W), visible light irradiation (light, $\lambda \geq 420$ nm) and their simultaneous superposition (light + ultrasonic, $\lambda \geq 420$ nm + 200 W), respectively. Under ultrasonic vibration condition, the control tests displayed that trace amount of H_2 (Fig. S9) could be detected with only pure water, only sacrificial agent as well as sacrificial agent and catalysts, indicating that ultrasound could not directly promote hydrogen production of catalysts [25]. Fig. 10a illustrated hydrogen production rates of CdS, $Mn_{0.2}Cd_{0.8}S$ and $Ni/Mn_{0.2}Cd_{0.8}S$ under light as well as simultaneous light and ultrasonic. Obviously, $Mn_{0.2}Cd_{0.8}S$ solid solution showed significantly enhanced photocatalytic and piezo-photocatalytic hydrogen production performance compared with CdS. In particular, the photocatalytic and piezo-photocatalytic performance of $Mn_{0.2}Cd_{0.8}S$ solid solution were 1.6 and 2.1 times that of CdS, respectively, indicating that the enhanced structural distortion by introducing Mn^{2+} in CdS was beneficial to the improvement of piezo-photocatalytic performance. After the modification with plasma metal Ni, the photocatalytic and piezo-photocatalytic hydrogen production performances of $Mn_{0.2}Cd_{0.8}S$ were obviously boosted, and the both performances over $Ni/Mn_{0.2}Cd_{0.8}S$ rose first and fell later as Ni content was gradually increased, which may be attributed to the excessive Ni hindering the capture of light and mechanical energy and also reducing the exposure of active sites. Particularly, the 1.5 wt %-$Ni/Mn_{0.2}Cd_{0.8}S$ displayed the highest photocatalytic (48.04 mmol g^{-1} h^{-1}) and piezo-photocatalytic (72.83 mmol g^{-1} h^{-1}) performance, approximately 13.0 and 11.8-folds those of $Mn_{0.2}Cd_{0.8}S$, respectively, and the piezo-photocatalytic activity was also better than that of other piezo-photocatalysts reported (Fig. 10e left and Table S6), indicating the obvious advantage of coupling piezoelectric and LSPR

effect for improving photocatalytic hydrogen evolution. Furthermore, the photostability and piezo-photostability of 1.5 wt%-$Ni/Mn_{0.2}Cd_{0.8}S$ were performed by five cyclic experiments, as displayed in Fig. 10b. After five continuous photocatalytic and piezo-photocatalytic cycles, the hydrogen production rates could maintain 87% and 88% of amount after the first cycle, respectively, which proved that the catalyst could be used continuously. The XRD pattern and SEM image of 1.5 wt %-$Ni/Mn_{0.2}Cd_{0.8}S$ after reaction for 15 h were presented in Fig. S10, further supporting the fact of excellent stability.

The wavelength dependence experiments of $Mn_{0.2}Cd_{0.8}S$ and 1.5 wt %-$Ni/Mn_{0.2}Cd_{0.8}S$ were tested to further clarify the influence of Ni LSPR on the photocatalytic/piezo-photocatalytic performance. From the results given in Fig. S11 and Fig. 10c, it could be seen that the photocatalytic and piezo-photocatalytic performances of 1.5 wt% $Ni/Mn_{0.2}Cd_{0.8}S$ were significantly enhanced compared with those of $Mn_{0.2}Cd_{0.8}S$ at the illumination wavelengths smaller than 550 nm, and both the photocatalytic and piezo-photocatalytic performances of 1.5 wt % $Ni/Mn_{0.2}Cd_{0.8}S$ and $Mn_{0.2}Cd_{0.8}S$ were steeply decreased when the bandpass wavelengths were equal to or larger than 550 nm. The enhanced catalytic performance of 1.5 wt% $Ni/Mn_{0.2}Cd_{0.8}S$ was mainly caused by the Ni LSPR effect, which could enhance the light absorption and generate hot electrons to boost the photocatalytic process. And the change of catalytic performance with the bandpass wavelengths was related to both the incident light energy and photocatalyst band-gap. The photon energy was decreased with increasing bandpass wavelength from 420 to 550 nm, and the later was around the absorption edges of $Mn_{0.2}Cd_{0.8}S$ and 1.5 wt%-$Ni/Mn_{0.2}Cd_{0.8}S$, which were calculated to be 544 and 551 nm, respectively, according to their band gaps. Therefore, no band gap absorption happened at illuminating wavelength greater than 550 nm, all of which resulted in the steep decrease of photocatalytic performances. The variation of photocatalytic performances at bandpass wavelengths ≥ 550 nm in Fig. 10c and Fig. S11
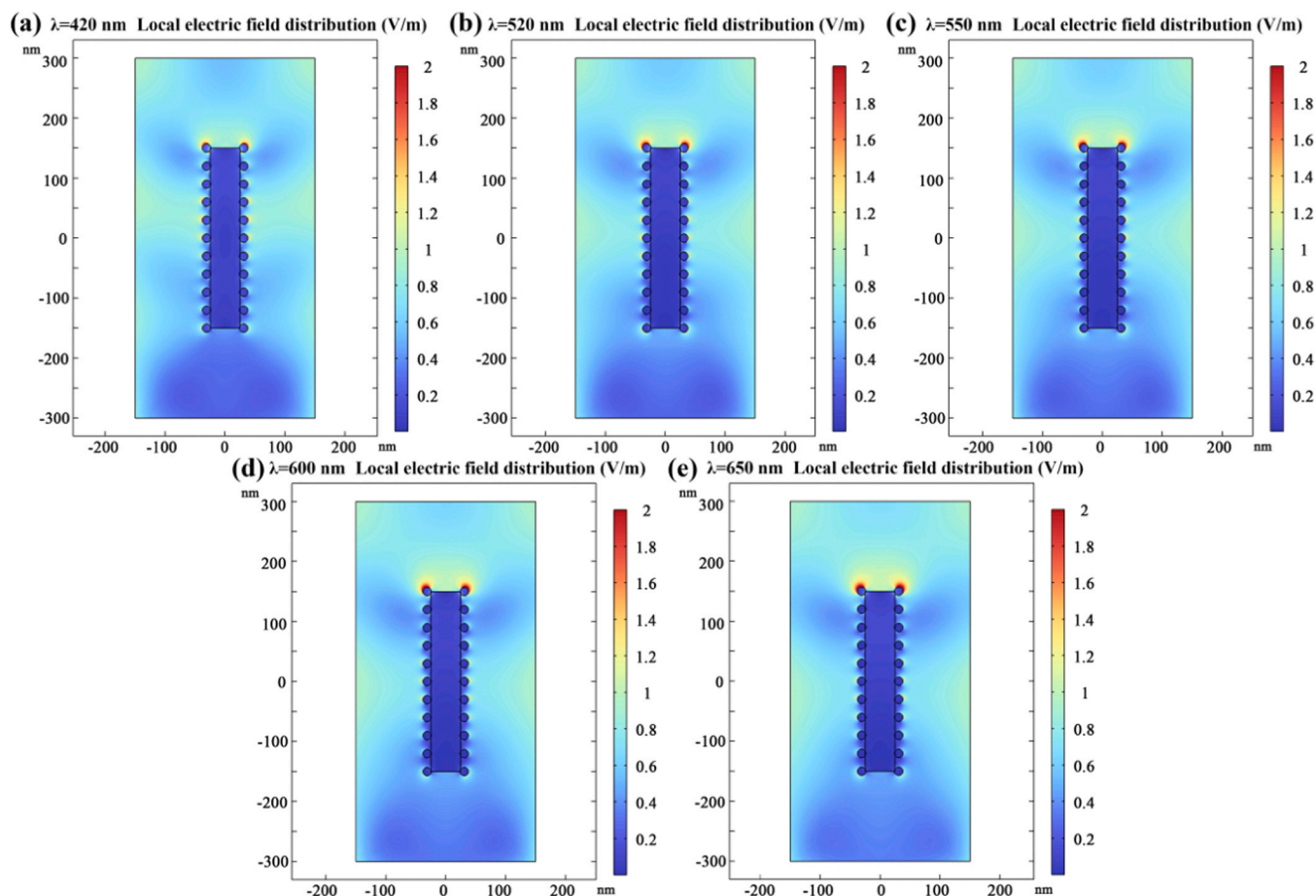
Fig. 8. The local electric field distribution maps of plasma metal Ni on the $Mn_{0.2}Cd_{0.8}S$ nanorods at the different monochromatic light.

could be explained as follows. Under only illumination condition (Fig. S11), $Mn_{0.2}Cd_{0.8}S$ could generate a certain amount of hydrogen (0.06 mmol g^{-1}) through band gap transition at 550 nm, while no band gap transition could occur at wavelength greater than 550 nm, so hydrogen could not be detected. For 1.5 wt%-Ni/$Mn_{0.2}Cd_{0.8}S$, apart from the band gap transition at 550 nm, owing to the wide-spectrum range of Ni LSPR [35–39], hot electrons were generated by plasma oscillation and transferred to the conduction band of $Mn_{0.2}Cd_{0.8}S$ to participate in the reduction of H_2O to H_2, therefore, a hydrogen evolution of 0.24 mmol g^{-1} could be detected at the wavelength of 550 nm, as well as that of 0.09 and 0.03 mmol g^{-1} still be detected at 600 and 650 nm, respectively. When the bandpass wavelength was 700 nm, no hydrogen was produced for 1.5 wt%-Ni/$Mn_{0.2}Cd_{0.8}S$, which was probably because the low-energy/density LSPR-excitation at 700 nm was difficult to induce the "hot electrons" injection process [54,55], so there was no hot electrons transfered to the conduction band of $Mn_{0.2}Cd_{0.8}S$ for hydrogen evolution reaction. Under illumination and ultrasound conditions (Fig. 10c), the piezoelectric polarization field generated by $Mn_{0.2}Cd_{0.8}S$ could promote the separation of photogenerated charge generated at 550 nm, so $Mn_{0.2}Cd_{0.8}S$ exhibited obvious piezo-photocatalytic hydrogen production performance (0.12 mmol g^{-1}). However, when the wavelengths were greater than 550 nm, only a small amount of hydrogen (0.03 mmol g^{-1}) could be detected due to the piezoelectric polarization water splitting. Because of the synergistic effect of band gap absorption, piezoelectric polarization and Ni plasma effect, 1.5 wt%-Ni/$Mn_{0.2}Cd_{0.8}S$ showed relatively high piezo-photocatalytic hydrogen production performance (0.33 mmol g^{-1}) under 550 nm irradiation, and could maintain a hydrogen evolution of 0.12 mmol g^{-1} when the wavelengths were greater than 550 nm until 650 nm due to the piezoelectric polarization

and Ni plasma effect. As the wavelength reached to 700 nm, the hydrogen evolution amount of 1.5 wt%-Ni/$Mn_{0.2}Cd_{0.8}S$ (0.03 mmol g^{-1}) was equal to that of $Mn_{0.2}Cd_{0.8}S$, indicating no hot electrons were transferred to the conduction band of $Mn_{0.2}Cd_{0.8}S$, which was similar to the situation of only illumination condition at the wavelengths of 700 nm for 1.5 wt%-Ni/$Mn_{0.2}Cd_{0.8}S$. Furthermore, by comparing the photocatalytic hydrogen production performances of 1.5 wt%-Ni/$Mn_{0.2}Cd_{0.8}S$ at same wavelengths for the two circumstances, it could be seen that the photocatalytic performance with the piezoelectric polarization was higher than that without it, which reflected the influence of piezoelectric polarization on the hydrogen production. In addition, the photocatalytic and piezo-photocatalytic hydrogen evolution of $Mn_{0.2}Cd_{0.8}S$ and 1.5 wt%-Ni/$Mn_{0.2}Cd_{0.8}S$ were further measured at $\lambda \geq 630$ nm (Fig. S12), the behaviors of hydrogen evolution exhibited at different conditions also verified the above discussion.

Considering the potential of plasmon piezo-photocatalysts for practical application, we also studied the processability of Ni/$Mn_{0.2}Cd_{0.8}S$ in the preparation of photosynthetic devices under the same test conditions. As shown in Fig. S13, 1.5 wt%-Ni/$Mn_{0.2}Cd_{0.8}S$ and ethyl cellulose aqueous dispersion (1 mg/mL) were cast onto circular filter paper (28.3 cm^2) to prepare thin Ni/$Mn_{0.2}Cd_{0.8}S$ film. The H_2 production over these films increased significantly with the number of drop-casting cycles (Fig. 10d). Remarkably, the highest H_2 production rate achieved to 92.84 mmol h^{-1} m^{-2}, which was better than that of most reported film devices (Fig. 10e right and Table S7). The gas produced by the 1.5 wt %-Ni/$Mn_{0.2}Cd_{0.8}S$ film under ultrasonic and light conditions was displayed by inflating a connected balloon and the videos were recorded (Video S1-S5). The exceptionally excellent piezo-photocatalytic hydrogen evolution performance of Ni/$Mn_{0.2}Cd_{0.8}S$ film demonstrated

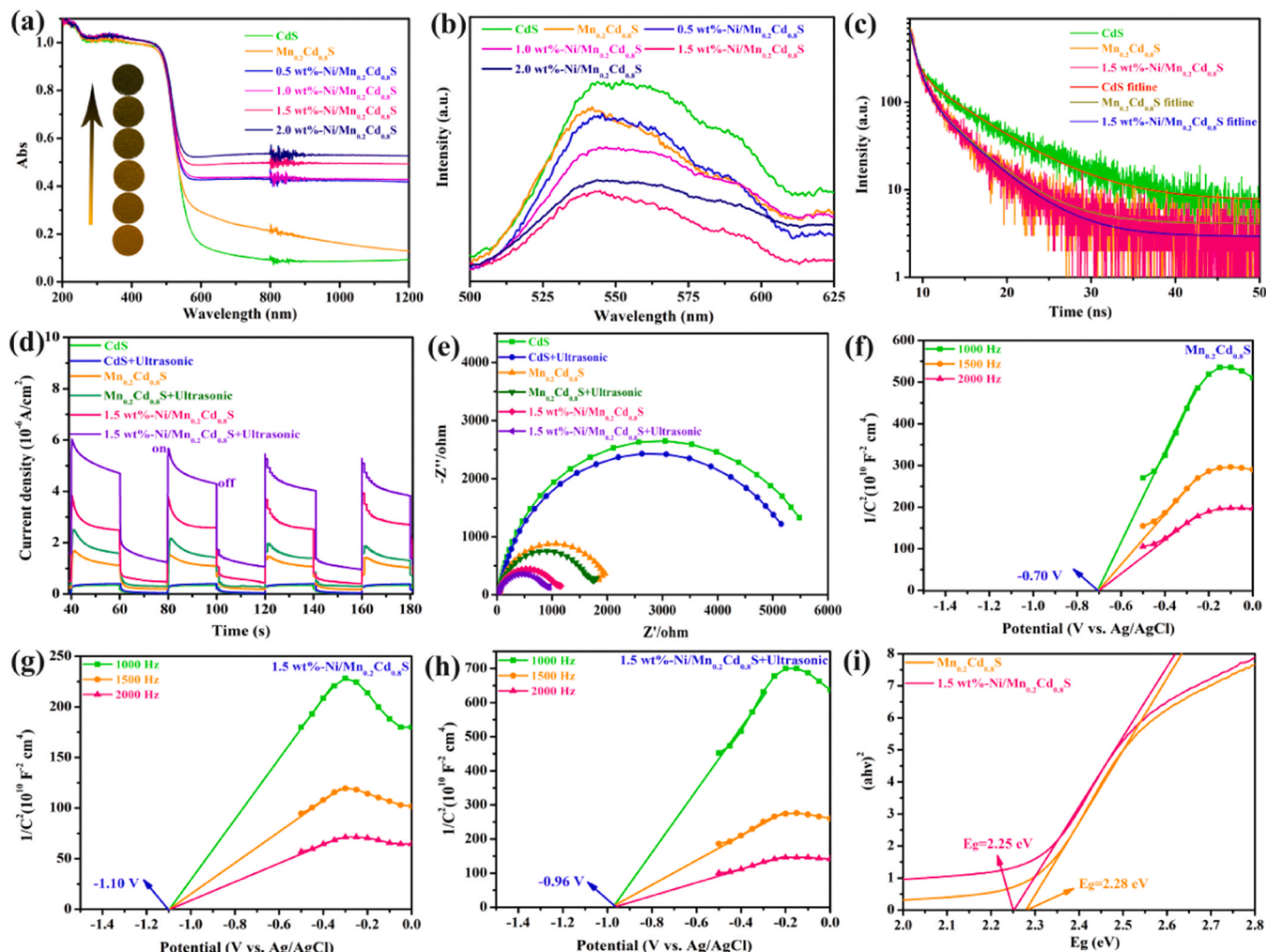**Fig. 9.** (a) UV-Vis-NIR DRS spectra of CdS, $Mn_{0.2}Cd_{0.8}S$ and $Ni/Mn_{0.2}Cd_{0.8}S$, (b) PL spectra of CdS, $Mn_{0.2}Cd_{0.8}S$ and $Ni/Mn_{0.2}Cd_{0.8}S$, (c) TRPL spectra of CdS, $Mn_{0.2}Cd_{0.8}S$ and 1.5 wt%-$Ni/Mn_{0.2}Cd_{0.8}S$, (d) I-t curves and (e) EIS Nyquist plots of CdS, $Mn_{0.2}Cd_{0.8}S$ and 1.5 wt%-$Ni/Mn_{0.2}Cd_{0.8}S$ under with and without ultrasonic. (f,g) Mott-Schottky plots of $Mn_{0.2}Cd_{0.8}S$ and 1.5 wt%-$Ni/Mn_{0.2}Cd_{0.8}S$ without ultrasonic. (h) Mott-Schottky plots of 1.5 wt%-$Ni/Mn_{0.2}Cd_{0.8}S$ with ultrasonic. (i) Band-gap of $Mn_{0.2}Cd_{0.8}S$ and 1.5 wt%-$Ni/Mn_{0.2}Cd_{0.8}S$.

that it has a great potential for the practical application.

Supplementary material related to this article can be found online at doi:10.1016/j.apcatb.2024.123809.

3.7. Possible piezo-photocatalytic enhanced mechanism of Ni/Mn$_{0.2}$Cd$_{0.8}$S

Based on the above experimental and calculations results, a reasonable piezo-photocatalytic hydrogen evolution mechanism for $Ni/Mn_{0.2}Cd_{0.8}S$ composites was proposed, as presented in Fig. 11. When $Mn_{0.2}Cd_{0.8}S$ were contacted with plasma metal Ni, the electrons in $Mn_{0.2}Cd_{0.8}S$ diffused to plasma metal Ni to reach an equilibrium state of the Fermi level and the energy band of $Mn_{0.2}Cd_{0.8}S$ bent upward (Fig. 11a), resulting in the formation of Schottky barriers [42]. Under the illumination of visible light, $Mn_{0.2}Cd_{0.8}S$ generated photoinduced electrons and holes, while plasma metal Ni produced hot electrons due to the induced collective oscillations of surface electrons [32]. The hot electrons generated by plasma metal Ni crossed the Schottky barrier to the conduction band of $Mn_{0.2}Cd_{0.8}S$, and then together with the photoinduced electrons of $Mn_{0.2}Cd_{0.8}S$ to participate in the reduction of H_2O to H_2, while photoinduced holes and hot holes were consumed by sacrificial reagents (Fig. 11b). However, due to the high Schottky barrier at the contact interface, the flow of hot electrons was hindered, resulting

in low transfer rate of hot electrons [32]. When the piezoelectric polarization field was introduced, the polarization charges were produced at the surface of $Mn_{0.2}Cd_{0.8}S$, which would dissipate the free electrons at the interface of $Mn_{0.2}Cd_{0.8}S$ and Ni, decreasing the degree of upward bending of the band, and thus reducing the Schottky barrier height [40, 56,57] (Fig. 11c). Under simultaneous light and ultrasonic, the reduced Schottky barrier improved the transfer efficiency of hot electrons from Ni to the neighboring $Mn_{0.2}Cd_{0.8}S$, leading to significantly enhanced photocatalytic activity (Fig. 11d). Therefore, though the reasonable couple of piezoelectric and LSPR effect, the Schottky barrier of $Ni/Mn_{0.2}Cd_{0.8}S$ can be tuned for promoting hot electrons transfer and achieving efficient hydrogen evolution performance.

4. Conclusion

In conclusion, the $Ni/Mn_{0.2}Cd_{0.8}S$ plasmon piezo-photocatalysts were constructed by combining plasma metal Ni with structural distortion-enhanced $Mn_{0.2}Cd_{0.8}S$ for piezo-photocatalytic hydrogen evolution. The piezoelectric polarization field generated by $Mn_{0.2}Cd_{0.8}S$ with ultrasonic wave could reduce the Schottky barrier height at the interface between Ni and $Mn_{0.2}Cd_{0.8}S$, thus promoting the transfer of plasma hot electrons and enhancing the piezo-photocatalytic hydrogen evolution performance. Under simultaneous illumination and
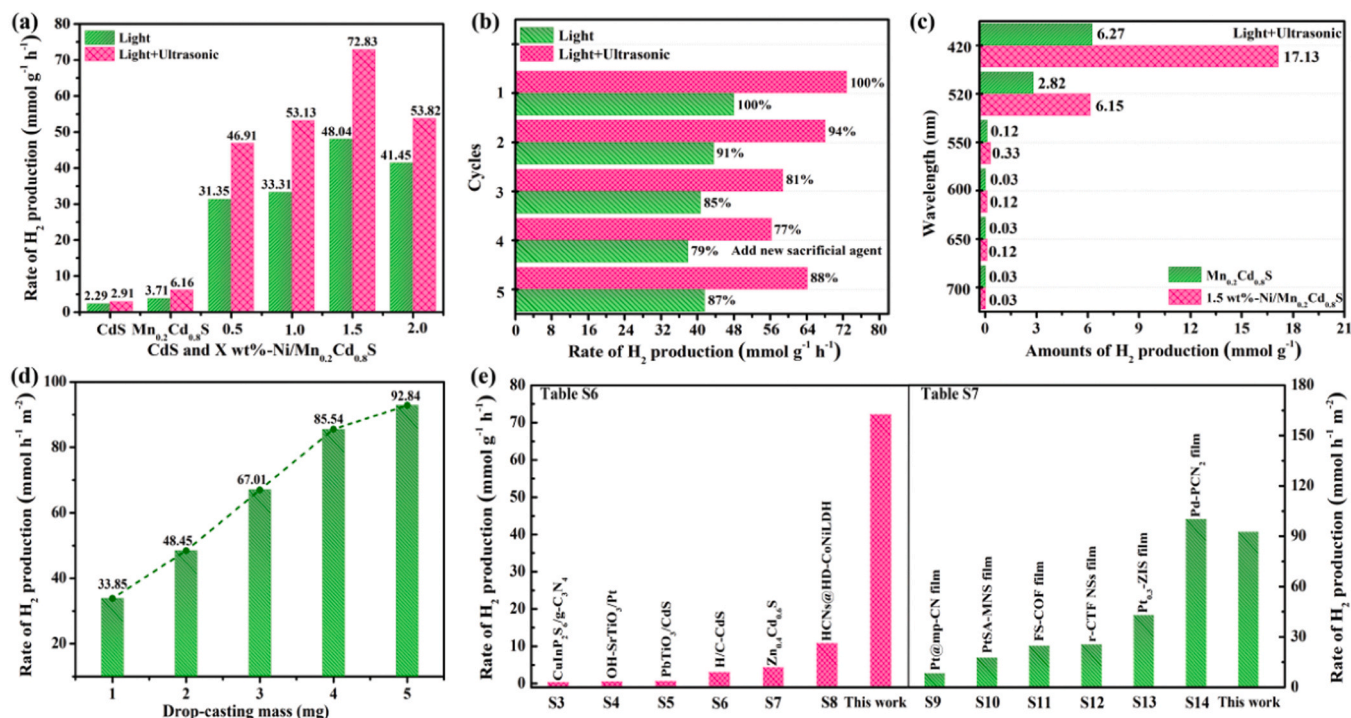
Fig. 10. (a) the hydrogen production rates of CdS, $Mn_{0.2}Cd_{0.8}S$ and $Ni/Mn_{0.2}Cd_{0.8}S$ under light as well as simultaneous light and ultrasonic. (b) cycling tests of photocatalytic and piezo-photocatalytic hydrogen production over 1.5 wt%-$Ni/Mn_{0.2}Cd_{0.8}S$. (c) wavelength dependence test of $Mn_{0.2}Cd_{0.8}S$ and 1.5 wt%-$Ni/Mn_{0.2}Cd_{0.8}S$ under simultaneous light and ultrasonic. (d) H_2 production rate for 1.5 wt%-$Ni/Mn_{0.2}Cd_{0.8}S$ film device with different drop-casting mass. (e) comparison of the piezo-photocatalytic hydrogen production activity for 1.5 wt%-$Ni/Mn_{0.2}Cd_{0.8}S$ and 1.5 wt%-$Ni/Mn_{0.2}Cd_{0.8}S$ film device with reported catalysts, originating from Table S6 and Table S7.
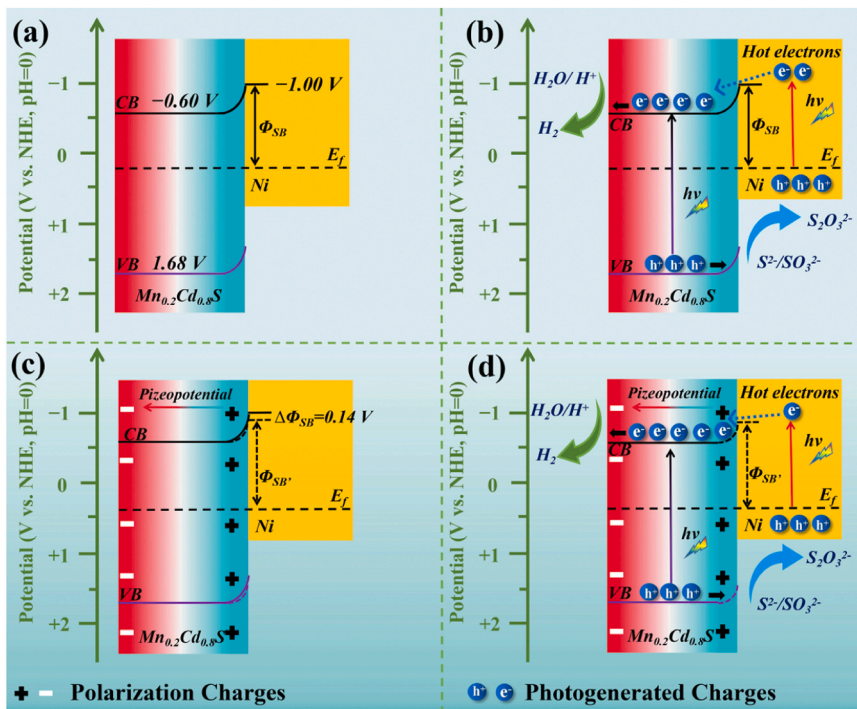

Fig. 11. Schematic diagram of synergistic enhancement of photocatalytic hydrogen production by coupling piezoelectric and LSPR effect.

ultrasound, the optimized 1.5 wt%-$Ni/Mn_{0.2}Cd_{0.8}S$ composite displayed ultrahigh piezo-photocatalytic hydrogen evolution rate of 72.38 mmol g^{-1} h^{-1}, which was approximately 11.8 and 25.0-fold that of $Mn_{0.2}Cd_{0.8}S$ and CdS, respectively. The significantly boosted

photocatalytic performance for $Ni/Mn_{0.2}Cd_{0.8}S$ composites were ascribed to the enhanced structural distortion of $Mn_{0.2}Cd_{0.8}S$ solid solution and the reasonably coupling the piezoelectric effect of $Mn_{0.2}Cd_{0.8}S$ with the LSPR of plasma metal Ni. This study highlights the

coordination mechanism of piezoelectric and LSPR effect in enhancing photocatalytic hydrogen evolution performance, and provides a reliable reference for developing high-performance plasmonic piezo-photocatalysts.

CRediT authorship contribution statement

Yongpan Gu: Investigation, Visualization. **Zhongjun Li:** Writing – review & editing. **Yike Li:** Writing – review & editing, Supervision. **Yanan Han:** Investigation, Visualization. **Haoqiang Feng:** Writing – original draft, Conceptualization, Investigation, Methodology, Validation.

Declaration of Competing Interest

The authors declare that they have no known competing financial interests or personal relationships that could have appeared to influence the work reported in this paper.

Data availability

Data will be made available on request.

Acknowledgement

Appendix A. Supporting information

Supplementary data associated with this article can be found in the online version at doi:10.1016/j.apcatb.2024.123809.

References

[1] S. Chu, A. Majumdar, Opportunities and challenges for a sustainable energy future, Nature 488 (2012) 294–303.

[2] H. Tong, S. Ouyang, Y. Bi, N.T. Umezawa, M. Oshikiri, J. Ye, Nano-photocatalytic materials: possibilities and challenges, Adv. Mater. 24 (2012) 229–251.

[3] X. Chen, S. Shen, L. Guo, S. Mao, Semiconductor-based photocatalytic hydrogen generation, Chem. Rev. 110 (2010) 6503–6570.

[4] R. L, H. Zhang, M. Hong, J. Shi, X. Liu, X. Feng, Two Co(II)/Ni(II) complexes based on nitrogenous heterocyclic ligands as high-performance electrocatalysts for the hydrogen evolution reaction, Dalton Trans. 51 (2022) 3970–3976.

[5] L. Cheng, Q. Xiang, Y. Liao, H. Zhang, CdS-based photocatalysts, Energy Environ. Sci. 11 (2018) 1362–1391.

[6] J.A. Nasir, Z.U. Rehman, S.N.A. Shah, A. Khan, I.S. Butler, C.R.A. Catlow, Recent developments and perspectives in CdS-based photocatalysts for water splitting, J. Mater. Chem. A 8 (2020) 20752–20780.

[7] H. Song, S. Luo, H. Huang, B. Deng, J. Ye, Solar-driven hydrogen production: recent advances, challenges, and future perspectives, ACS Energy Lett. 7 (2022) 1043–1065.

[8] V.N. Rao, N.L. Reddy, M.M. Kumari, K.K. Cheralathan, P. Ravi, M. Sathish, B. Neppoliand, K.R. Reddy, N.P. Shetti, P. Prathap, T.M. Aminabhavi, M. V. Shankar, Sustainable hydrogen production for the greener environment by quantum dots-based efficient photocatalysts: a review, J. Environ. Manag. 248 (2019) 109246.

[9] T. Su, C. Men, L. Chen, B. Chu, X. Luo, H. Ji, J. Chen, Z. Qin, Sulfur vacancy and Ti$_3$C$_2$T$_x$ cocatalyst synergistically boosting interfacial charge transfer in 2D/2D Ti$_3$C$_2$T$_x$/ZnIn$_2$S$_4$ heterostructure for enhanced photocatalytic hydrogen evolution, Adv. Sci. 9 (2021) 2103715.

[10] Z. Yang, H. Li, S. Chen, S. Yang, F. Peng, J. Liao, Y. Fang, S. Zhang, S. Zhang, Cocatalyst engineering with robust tunable carbon encapsulated Mo-Rich Mo/ Mo$_2$C heterostructure nanoparticle for efficient photocatalytic hydrogen evolution, Adv. Funct. Mater. 33 (2023) 2212746.

[11] X. Li, Q. Liu, F. Deng, J. Huang, L. Han, C. He, Z. Chen, Y. Luo, Y. Zhu, Double-defect-induced polarization enhanced O$_V$-BiOBr/Cu$_{2-x}$S high-low junction for boosted photoelectrochemical hydrogen evolution, Appl. Catal. B Environ. 314 (2022) 121502.

[12] S. Tu, Y. Guo, Y. Zhang, C. Hu, T. Zhang, T. Ma, H. Huang, Piezocatalysis and piezo-photocatalysis: catalysts classification and modification strategy, reaction mechanism, and practical application, Adv. Funct. Mater. 30 (2020) 2005158.

[13] Z. Liu, X. Yu, L. Li, Piezopotential augmented photo- and photoelectro-catalysis with a built-in electric field, Chin. J. Catal. 41 (2020) 534–549.

[14] T. Lv, J. Li, N. Arif, L. Qi, J. Lu, Z. Ye, Y. Zeng, Polarization and external-field enhanced photocatalysis, Matter 5 (2022) 1–37.

[15] J. Liu, W. Qi, M. Xu, T. Thomas, S. Liu, M. Yang, Piezocatalytic techniques in environmental remediation, Angew. Chem. Int. Ed. 62 (2023) e202213927.

[16] C. Hu, S. Tu, N. Tian, T. Ma, Y. Zhang, H. Huang, Photocatalysis enhanced by external fields, Angew. Chem. Int. Ed. 60 (2021) 16309–16328.

[17] H. Zheng, Y. Wang, J. Liu, J. wang, K. Yan, K. Zhu, Recent advancements in the use of novel piezoelectric materials for piezocatalytic and piezo-photocatalytic applications, Appl. Catal. B Environ. 341 (2024) 123335.

[18] R. Mohanty, S. Mansingh, K. Parida, K. Parida, Boosting sluggish photocatalytic hydrogen evolution through piezo-stimulated polarization: a critical review, Mater. Horiz. 9 (2022) 1332–1355.

[19] C. Yang, Y. Chen, T. Chen, Y. Hao, S. Rajendran, Z. Zeng, Q. Sun, J. Qin, X. Zhang, A long-standing polarized electric field in TiO$_2$@BaTiO$_3$/CdS nanocomposite for effective photocatalytic hydrogen evolution, Fuel 314 (2022) 122758.

[20] Y. Jiang, J. Xie, Z. Lu, J. Hu, A. Hao, Y. Cao, Insight into the effect of OH modification on the piezo-photocatalytic hydrogen production activity of SrTiO$_3$, J. Colloid Interf. Sci. 612 (2022) 111–120.

[21] X. Huang, R. Lei, J. Yuan, F. Gao, C. Jiang, W. Feng, J. Zhuang, P. Liu, Insight into the piezo-photo coupling effect of PbTiO$_3$/CdS composites for piezo-photocatalytic hydrogen production, Appl. Catal. B Environ. 282 (2021) 119586.

[22] B. Lin, A. Chaturvedi, J. Di, L. You, C. Lai, R. Duan, J. Zhou, B. Xu, Z. Chen, P. Song, J. Peng, B. Ma, H. Liu, P. Meng, G. Yang, H. Zhang, Z. Liu, F. Liu, Ferroelectric-field accelerated charge transfer in 2D CuInP$_2$S$_6$ heterostructure for enhanced photocatalytic H$_2$ evolution, Nano Energy 76 (2020) 104972.

[23] M. Zhang, S. Nie, T. Cheng, Y. Feng, C. Zhang, L. Zheng, L. Wu, W. Hao, Y. Ding, Enhancing the macroscopic polarization of CdS for piezo-photocatalytic water splitting, Nano Energy 90 (2021) 106635.

[24] J. Zhang, S. Wageh, A. Al-Ghamdi, J. Yu, New understanding on the different photocatalytic activity of wurtzite and zinc-blende CdS, Appl. Catal. B Environ. 192 (2016) 101–107.

[25] Y. Zhao, Z. Fang, W. Feng, K. Wang, X. Huang, P. Liu, Hydrogen production from pure water via piezoelectric-assisted visible-light photocatalysis of CdS nanorod arrays, ChemCatChem 10 (2018) 3397–3401.

[26] J. Wang, C. Hu, Y. Zhang, H. Huang, Engineering piezoelectricity and strain sensitivity in CdS to promote piezocatalytic hydrogen evolution, Chin. J. Catal. 43 (2022) 1277–1285.

[27] Q. Zhao, Y. Zou, Z. Liu, The spontaneous polarization in CdS to enhance the piezo-PEC performance via phase transition stress engineering, J. Catal. 416 (2022) 398–409.

[28] S. Lin, S. Li, H. Huang, H. Yu, Y. Zhang, Synergetic piezo-photocatalytic hydrogen evolution on Cd$_x$Zn$_{1-x}$S solid-solution 1D nanorods, Small 18 (2022) 2106420.

[29] D. Xiang, Z. Liu, M. Wu, H. Liu, X. Zhang, Z. Wang, Z. Wang, L. Li, Enhanced piezo-photoelectric catalysis with oriented carrier migration in asymmetric Au−ZnO nanorod array, Small 16 (2020) 1907603.

[30] L. Guo, C. Zhong, J. Cao, Y. Hao, M. Lei, K. Bi, Q. Sun, Z.L. Wang, Enhanced photocatalytic H$_2$ evolution by plasmonic and piezotronic effects based on periodic Al/BaTiO$_3$ heterostructures, Nano Energy 62 (2019) 513–520.

[31] S. Li, Z. Zhao, M. Liu, X. Liu, W. Huang, S. Sun, Y. Jiang, Y. Liu, J. Zhang, Z. Zhang, Remarkably enhanced photocatalytic performance of Au/AgNbO$_3$ heterostructures by coupling piezotronic with plasmonic effects, Nano Energy 95 (2022) 107031.

[32] J. Li, G. Xie, J. Jiang, Y. Liu, C. Chen, W. Li, J. Huang, X. Luo, M. Xu, Q. Zhang, M. Yang, Y. Su, Enhancing photodegradation of methyl orange by coupling piezo-phototronic effect and localized surface plasmon resonance, Nano Energy 108 (2023) 108234.

[33] Y. Shi, L. Li, Z. Xu, F. Guo, Y. Li, W. Shi, Synergistic coupling of piezoelectric and plasmonic effects regulates the Schottky barrier in Ag nanoparticles/ultrathin g-C$_3$N$_4$ nanosheets heterostructure to enhance the photocatalytic activity, Appl. Surf. Sci. 616 (2023) 156466.

[34] C.Y. Tu, J.M. Wu, Localized surface plasmon resonance coupling with piezophototronic effect for enhancing hydrogen evolution reaction with Au@MoS$_2$ nanoflowers, Nano Energy 87 (2021) 106131.

[35] Z. Xin, L. Lu, B. Wang, X. Wang, K. Zhu, Z. Xu, Z. Yu, S. Yan, Z. Zou, Lewis acid activated CO$_2$ reduction over a Ni modified Ni−Ge hydroxide driven by visible infrared light, Dalton Trans. 48 (2019) 1672–1679.

[36] H. Liu, T.D. Dao, L. Liu, X. Meng, T. Nagao, J. Ye, Light assisted CO$_2$ reduction with methane over group VIII metals:universality of metal localized surface plasmon resonance in reactant activation, Appl. Catal. B Environ. 209 (2017) 183–189.

[37] G.S. Pawar, A. Elikkottil, B. Pesala, A.A. Tahir, T.K. Mallick, Plasmonic nickel nanoparticles decorated on to LaFeO$_3$ photocathode for enhanced solar hydrogen generation, Int. J. Hydrog. Energy 44 (2019) 578–586.

[38] L. Pei, T. Li, Y. Yuan, T. Yang, J. Zhong, Z. Ji, S. Yan, Z. Zou, Schottky junction effect enhanced plasmonic photocatalysis by TaON@Ni NP heterostructures, Chem. Commun. 55 (2019) 11754–11757.

[39] S. He, J. Huang, J.L. Goodsell, A. Angerhofer, W.D. Wei, Plasmonic Nickel-TiO$_2$ heterostructures for visible-light-driven photochemical reactions, Angew. Chem. Int. Ed. 58 (2019) 6038–6041.

[40] L. Pan, S. Sun, Y. Chen, P. Wang, J. Wang, X. Zhang, J. Zou, Z. Wang, Advances in piezo-phototronic effect enhanced photocatalysis and photoelectrocatalysis, Adv. Energy Mater. 10 (2020) 2000214.

[41] Z. Liang, C.F. Yan, S. Rtimi, F. Guo, J. Bandara, Piezoelectric materials for catalytic/photocatalytic removal of pollutants: Recent advances and outlook, Appl. Catal. B Environ. 241 (2019) 256–269.

[42] J. Xu, T. Qin, W. Chen, J. Lv, X. Zeng, J. Sun, Y. Li, J. Zhou, Synergizing piezoelectric and plasmonic modulation of Ag/BiFeO$_3$ fibrous heterostructure toward boosted photoelectrochemical energy conversion, Nano Energy 89 (2021) 106317.

[43] Q. Liu, Z. Li, J. Li, F. Zhan, D. Zhai, Q. Sun, Z. Xiao, H. Luo, D. Zhang, Three dimensional BaTiO$_3$ piezoelectric ceramics coated with TiO$_2$ nanoarray for high performance of piezo-photoelectric catalysis, Nano Energy 98 (2022) 107267.

[44] Q. Huang, Y. Xiong, Q. Zhang, H. Yao, Z. Li, Noble metal-free MoS$_2$ modified Mn$_{0.25}$Cd$_{0.75}$S for highly efficient visible-light driven photocatalytic H$_2$ evolution, Appl. Catal. B Environ. 209 (2017) 514–522.

[45] L. Li, G. Liu, S. Qi, X. Liu, L. Gu, Y. Lou, J. Chen, Y. Zhao, Highly efficient colloidal Mn$_x$Cd$_{1-x}$S nanorod solid solution for photocatalytic hydrogen generation, J. Mater. Chem. A 6 (2018) 23683–23689.

[46] Q. Huang, Z. Tao, L. Ye, H. Yao, Z. Li, Mn$_{0.2}$Cd$_{0.8}$S nanowires modified by CoP$_3$ nanoparticles for highly efficient photocatalytic H$_2$ evolution under visible light irradiation, Appl. Catal. B Environ. 237 (2018) 689–698.

[47] C. Cheng, J. Zhang, R. Zeng, F. Xing, C. Huang, Schottky barrier tuning via surface plasmon and vacancies for enhanced photocatalytic H$_2$ evolution in seawater, Appl. Catal. B Environ. 310 (2022) 121321.

[48] Z. Chai, T.T. Zeng, Q. Li, L.Q. Lu, W.J. Xiao, D. Xu, Efficient Visible light-driven splitting of alcohols into hydrogen and corresponding carbonyl compounds over a Ni-Modified CdS photocatalyst, J. Am. Chem. Soc. 138 (2016) 10128–10131.

[49] A. Luna, E. Novoseltceva, E. Louarn, P. Beaunier, E. Kowalska, E. Kowalska, M. Valenzuela, H. Remita, C. Colbeau-Justin, Synergetic effect of Ni and Au nanoparticles synthesized on titania particles for efficient photocatalytic hydrogen production, Appl. Catal. B Environ. 191 (2016) 18–28.

[50] H. Yang, Z. Jin, K. Fan, D. Liu, G. Lu, The roles of Ni nanoparticles over CdS nanorods for improved photocatalytic stability and activity, Superlattices Microstruct. 111 (2017) 687–695.

[51] B. Fu, J. Li, H. Jiang, X. He, Y. Ma, J. Wang, C. Hu, Modulation of electric dipoles inside electrospun BaTiO$_3$@TiO$_2$ core-shell nanofibers for enhanced piezo-photocatalytic degradation of organic pollutants, Nano Energy 93 (2022) 106841.

[52] X. Zhou, F. Yan, S. Wu, B. Shen, C. Jiang, H. Zeng, J. Zhuang, J. Zhai, Remarkable piezophoto coupling catalysis behavior of BiO$_X$/BaTiO$_3$ (X = Cl, Br, Cl$_{0.166}$Br$_{0.834}$) piezoelectric composites, Small 16 (2020) 2001573.

[53] H. Liu, R. Zhu, N. Shi, L. Zhang, S. Li, J. Zhang, Piezotronic effect induced schottky barrier decrease to boost the plasmonic charge separation of BaTiO$_3$-Au heterojunction for the photocatalytic selective oxidation of aminobenzyl alcohol, ACS Appl. Mater. Interfaces 14 (2022) 55548–55558.

[54] Z. Zhang, J. Huang, Y. Fang, M. Zhang, K. Liu, B. Dong, A nonmetal plasmonic Z-Scheme photocatalyst with UV-to-NIR-Driven photocatalytic protons reduction, Adv. Mater. 29 (2017) 1606688.

[55] W. Xue, H. Sun, X. Hu, X. Bai, J. Fan, E. Liu, UV-VIS-NIR-induced extraordinary H$_2$ evolution over W$_{18}$O$_{49}$/Cd$_{0.5}$Zn$_{0.5}$S: surface plasmon effect coupled with S-scheme charge transfers, Chin. J. Catal. 43 (2022) 234–245.

[56] X. Zhou, B. Shen, A. Lyubartsev, J. Zhai, N. Hedin, Semiconducting piezoelectric heterostructures for piezo and piezophotocatalysis, Nano Energy 96 (2022) 107141.

[57] B. Dai, G. Biesold, M. Zhang, H. Zou, Y. Ding, Z. Wang, Z. Lin, Piezo-phototronic effect on photocatalysis, solar cells, photodetectors and light-emitting diodes, Chem. Soc. Rev. 50 (2021) 13646–13691.